Acoustic Wind Tunnel Measurements of a Quadcopter in Hover and Forward Flight Conditions

Nikolas S. Zawodny*
Nicole A. Pettingill†
Aeroacoustics Branch
NASA Langley Research Center
Hampton, VA 23681

ABSTRACT

An experimental testing campaign was conducted in the NASA Langley Low Speed Aeroacoustic Wind Tunnel (LSAWT) in order to better understand the acoustic characteristics of a representative quadcopter system in both hover and forward flight conditions. Aerodynamic performance measurements were acquired using a multi-axis load cell to trim the vehicle to desired thrust/lift conditions. Hover acoustic measurements provide evidence of prominent rotor-airframe interaction noise that manifests in the form of high-amplitude harmonics of the fundamental rotor blade passage frequency. Forward flight acoustic measurements of simultaneous rotor operations indicate the presence of strong forward-aft rotor wake interactions that yield increased broadband noise levels relative to cases of individual rotor operation. These results indicate the potential need for modeling complex noise generation mechanisms associated with multirotor and rotor-airframe interactions for vehicles of this class.

Keywords: Unmanned Aircraft Systems, Acoustics, Wind Tunnel Measurements
I-INCE Classification of Subjects Number(s): 19.6

1. INTRODUCTION

The past decade has shown a rapidly increased interest in the use of unmanned aircraft systems (UAS) for both recreational and commercial purposes. Of the first 1,000 commercial UAS exemptions granted by the FAA, 89% are of the multicopter variety.[1] Multirotor UAS present unique advantages over fixed-wing UAS, such as the ability to hover in place at a desired altitude for purposes such as visual surveillance or package delivery. These advantages, however, are accompanied by potential drawbacks such as the chance for prolonged exposure to the civilian population. In addition to visual exposure, the acoustic signature of these vehicles may not be acceptable to people. Depending on vehicle attributes such as size, weight, and mission profile, incorporation of acoustics into the vehicle design process may be warranted.

*nikolas.s.zawodny@nasa.gov
†nicole.a.pettingill@nasa.gov

It is therefore useful to assess the acoustic characteristics and primary noise-generating mechanisms of representative multirotor UAS.

Measurements of small UAS acoustics have been performed via outdoor flight testing of full vehicles as well as via indoor measurements of vehicle sub-components.[2–5] Acoustic measurements from vehicle outdoor flight testing are important since they represent the vehicle in realistic flight conditions. However, identification of the physical noise-generating mechanisms from flight test data is difficult. Furthermore, atmospheric variability such as temperature and winds can create additional data variance. Testing in a wind tunnel environment offers benefits for the purpose of noise source identification. These include the ability to isolate individual component noise contributions, and to provide an acoustically controlled environment suitable for providing stationary acoustic data more appropriate for initial predictive validations.

2. TECHNICAL APPROACH

2.1 The LSAWT

The LSAWT is an open-circuit free jet wind tunnel that is currently configured for a freestream Mach number range of $0.045 \leq M_\infty \leq 0.140$ and is reconfigurable to an upper end capability of $M_{\infty,\max} = 0.32$. The facility had recently undergone a capability enhancement for the purposes of acquiring aerodynamic performance and acoustic data of small electric propeller/rotor platforms and small UAS.[6] A cut-away illustration of the facility is provided in Fig. 1. The test chamber of the facility is acoustically treated with fiberglass wedges down to a cut-off frequency of approximately 200 Hz and is outfitted with a 28-element linear array of 6.35 mm-diameter B&K model 4939 free-field microphones. As Fig. 1 shows, the microphone array is oriented in the streamwise direction along one of the chamber upper corners. The length of the test section from inlet trailing edge to flow collector leading edge is approximately 5.6 m, and the diameter of the circular inlet nozzle, D_{nozzle}, is 1.93 m.

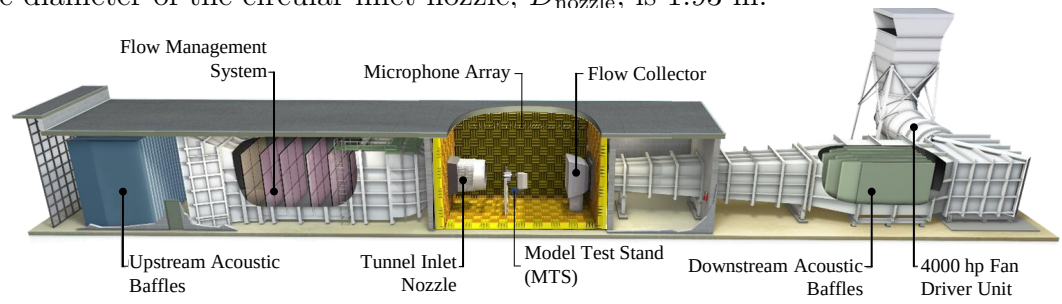

Figure 1: Rendered cut-away illustration of the LSAWT.

2.2 The Vehicle

The vehicle tested in this study is the Straight Up Imaging (SUI) Endurance quadcopter. Images of the vehicle mounted on the LSAWT model test stand (MTS) as well as the rotor directions of rotation are provided in Fig. 2. The vehicle primary geometric components include a faired airframe, four rotors, and a landing gear assembly. The rotors are powered by outrunning brushless motors, which are mounted at the ends of carbon fiber cylindrical rods

that protrude from the vehicle airframe. The vehicle forward rotors are herein referred to as R1 and R2, while the aft rotors are referred to as R3 and R4. The rotational sense of each rotor is such that it is counter-rotating relative to its neighboring rotors. The hub-to-hub distance between neighboring motors is approximately 510 mm (≈20 in.). Each rotor consists of two carbon fiber fixed-pitch blades, each with a blade radius of $R = 190.5$ mm.

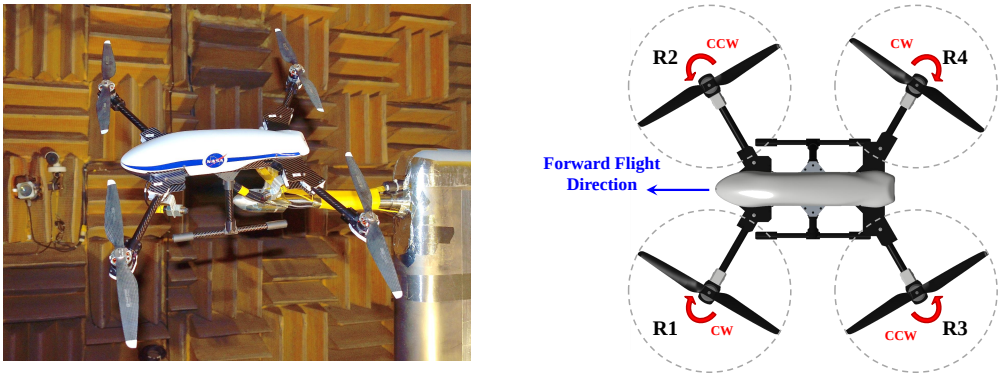

(a) Image of vehicle installed on MTS (b) Rotor nomenclature (top view)

Figure 2: The SUI Endurance quadcopter.

A schematic of a single itemized rotor-motor power system is provided in Fig. 3(a). As this figure shows, each motor-rotor system was controlled independently using a dedicated electronic speed controller (ESC). A single DC power supply was used to power all ESC-motor systems using a constant bus voltage of 16.5 Volts DC. Finally, each ESC received a dedicated pulse width modulation (PWM) signal from a multi-channel servo controller. All four ESCs were housed within the SUI Endurance airframe as shown in Fig. 3(b). While it is not shown in this image, a thermocouple was attached to one of the rear ESC housings to monitor its temperature during operations. One of the rear ESCs was chosen for monitoring because these rotors were anticipated to exhibit larger aerodynamic loads and thus draw higher currents in forward flight conditions than the forward rotors.

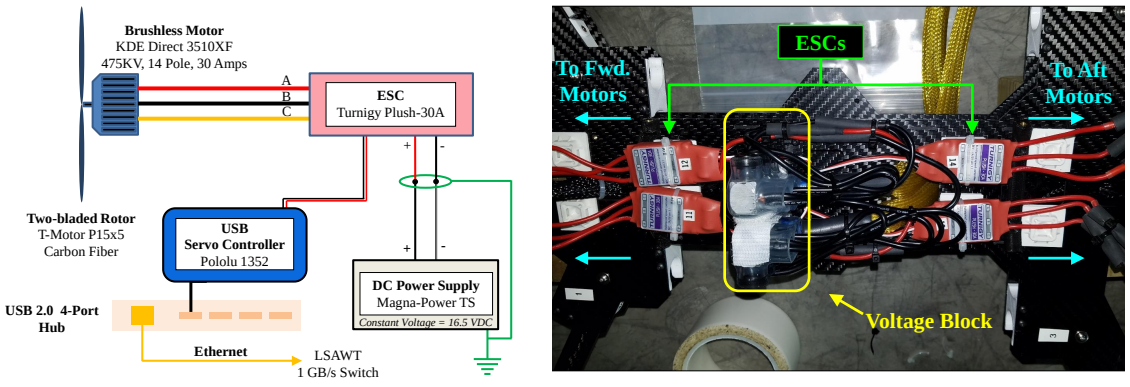

(a) (b)

Figure 3: The motor power supply chain for the SUI Endurance: (a) itemized single rotor-motor-ESC system schematic, (b) image of electronic components stored within airframe housing (top airframe shell removed).

2.3 Testing Conditions

The acoustic testing configurations are summarized in Fig. 4. As Fig. 4(a) shows, a total of four azimuthal microphone survey orientations were tested. These were accomplished by rotating the vehicle airframe on the MTS relative to the LSAWT linear microphone array. A fixed lateral separation distance of 3.54 m ($\approx 18.5R$) was maintained between the microphone elements and the center of the vehicle. The polar extents of the microphones are shown pictorially in Fig. 4(b). While this image presents the microphone array in the flyover configuration, the indicated range of microphone polar angles is applicable to all measured azimuthal orientations indicated in Fig. 4(a).

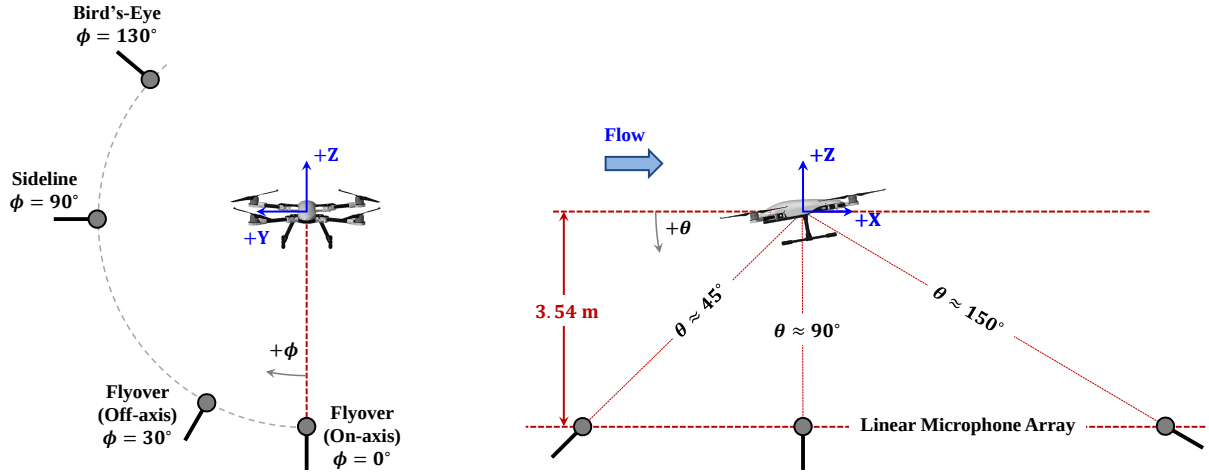

(a) Azimuthal (ϕ) locations of array surveys (b) Polar (θ) locations of flyover microphones

Figure 4: Linear microphone array survey orientations: (a) upstream view of azimuthal plane (flow is into page), (b) profile view of polar plane (flyover configuration). *(Note: images not drawn to scale)*

A checklist of available data for different motor/rotor configurations, the different microphone array orientations, and vehicle flight conditions is provided in Table 1. It is worth noting that the bird's-eye array orientation corresponds to the configuration in which the quadcopter was installed in an upright orientation on the MTS. It is this configuration for which load cell data were acquired, since it represented an orientation in which the vehicle

Table 1: Experimental testing conditions.

Array Orientation		**Rotor Operations**				**Flight Condition**	
Name	ϕ, deg.	Motor[1]	All	Indiv.	Pairs[2]	Hover	Fwd. Flight[3]
Flyover (On-axis)	0	✓	✓	✓	✓	✓	✓
Flyover (Off-axis)	30	✗	✓	✓	✓	✗	✓
Sideline	90	✗	✓	✓	✗	✓	✓
Bird's-Eye	130	✗	✓	✓	✗	✓	✓

[1]Represent individual, unloaded motor runs
[2]Only apply to fwd. flight conditions
[3]All forward flight runs performed at $M_\infty = 0.045$ and $\alpha_v = -10°$.

loads were most amenable to the load cell range capabilities. The load cell was removed for the other vehicle orientations.

As shown in Fig. 5(a), the load cell was mounted directly under the vehicle approximately in-line with the landing gear support legs. This location closely corresponds to the vehicle center of gravity. A rounded leading-edge strut was used to position the vehicle and load cell above the sting arm of the MTS. Four laser sensor tachometers (one per motor) were installed under the vehicle airframe and oriented towards the vehicle motor housings, which were outfitted with a strip of reflective tape. This allowed for tracking of both rotor positions and rotation rates for all test runs. Figure 5(b) provides an image of the global (LSAWT) and vehicle coordinate systems. The vehicle coordinate system is analogous to the measurement directions of the load cell, and represents a simple pitch rotation (α_v) of the global coordinate system about the Y axis (see Fig. 4). All hover and forward flight conditions were conducted at $\alpha_v = 0°$ and $\alpha_v = -10°$, respectively. All forward flight measurements were conducted at a tunnel freestream Mach number of $M_\infty = 0.045$ ($U_\infty \approx 15.5$ m/s).

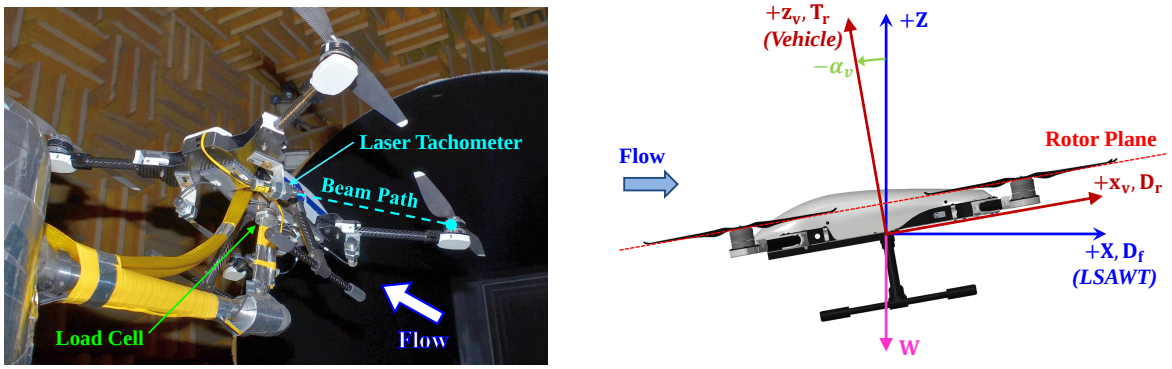

(a) Load cell and laser tachometer setup

(b) LSAWT and vehicle coordinate systems

Figure 5: Load cell and laser tachometer measurement setup and coordinate systems for vehicle mounted in upright orientation on MTS. *(Note: images represent vehicle in forward flight.)*

2.4 Data Acquisition & Processing

Dynamic data were acquired on National Instruments™ PXI-6143 dynamic signal acquisition modules installed across two PXI-1045 chassis. Microphone data were acquired on one of the chassis at a sampling rate of 80 kHz. Load cell data were acquired on the second chassis at a lower sampling rate of 40 kHz. Microphone and vehicle performance data acquisitions were divided between these two chassis to allow for real-time monitoring of the performance data to establish vehicle trim conditions. Microphone data were bandpass-filtered between high- and low-pass cut-off frequencies of 80 Hz and 40 kHz, respectively. This filtering provided a usable flat passband (less than −0.5 dB deviation) within a frequency range of 100 Hz $\leq f \leq$ 25 kHz. Each wind tunnel run was acquired for a time duration of 12 seconds.

Acoustic data were post-processed using three different techniques:[4,5]

1. Random dataset: narrowband acoustic spectra computed using fast Fourier Transform (FFT)

2. Unfiltered rotor revolution: Mean rotor revolution time history computed, subtracted from time record to retain random noise components

3. BPF harmonic-filtered data set: Acoustic time series filtered to retain only harmonics of BPF

The first of these techniques simply treats the acquired data as a random data set and computes narrowband acoustic spectra using the fast Fourier Transform (FFT). Acoustic spectra using this method were computed using a Hanning window with 75% overlap and a frequency resolution of 5 Hz. For 12 seconds of data, this results in an autospectral random uncertainty of $\epsilon_r = 9.0\%$, which translates to a random SPL uncertainty of $u_{r,\mathrm{SPL}} \in \{-0.41, +0.37\}$ dB.[7] Method 2 allows for the separation of periodic and random noise components in the time domain. Narrowband spectra are then computed on the mean revolution time history and residual random time series with a common frequency resolution of 5 Hz. Processing the mean and residual time series with a common frequency resolution required replicating the mean revolution time history by the number of revolution time blocks. Finally, method 3 is included to more accurately compare acoustic amplitudes between future predictions and experiments in the time domain. The reader is referred to Refs. 4, 5 for more detail on the latter two processing techniques.

Due to the potential refraction of sound waves through the open-jet shear layer, a cylindrical shear layer correction is applied to the wind tunnel microphone data for forward flight cases.[8] The result of this correction is both an amplitude correction in dB, L_c, and a physical microphone location correction in terms of source-to-microphone distance and polar angle, r_c and θ_c. Due to the low freestream velocity associated with these cases, the net amplitude corrections (L_{corr}) are found to be very small for all microphones when corrected for spherical spreading (within ± 0.5 dB). Meanwhile, the polar angle corrections (θ_{corr}) are computed to be within an upper limit of 3.2°. In other words,

$$|L_{\mathrm{corr}}| = |L_c + 20\log_{10}(r_c/r_o)| \leq 0.5 \text{ dB}, \tag{1}$$

and

$$\theta_{\mathrm{corr}} = \theta_c - \theta_o \leq 3.2^\circ, \tag{2}$$

where r_o and θ_o represent the geometric source-to-observer distance and polar directivity angle, respectively. Therefore, only the retarded microphone directivity angles, θ_c, are of practical importance when relating the microphone measurements to the geometric source-to-observer distances for this study. Note that no shear layer corrections are needed for hover conditions ($M_\infty = 0$).

Finally, three acoustic metrics are used in this study for both comparisons between flight conditions and between periodic and broadband noise contributions. They are the sound pressure level (SPL) spectrum, the overall sound pressure level (OASPL) denoted by L, and the A-weighted OASPL denoted by L_A.[9] All OASPLs are calculated over a frequency range of $100 \leq f \leq 20,000$ Hz unless indicated otherwise. In addition to narrowband spectra as discussed previously, some spectra will also be presented in 1/3rd octave bands $\left(\mathrm{SPL}_{1/3}\right)$ for visual clarity of trends.

3. RESULTS & INTERPRETATION

3.1 Hover vs. Forward Flight

The acoustic behavior of a rotor in hover is considerably different from that of the same rotor in edgewise forward flight. In hover, the rotor blade experiences nearly identical resultant velocity and angle of attack conditions as it rotates about the hub, resulting in a steady loading condition on the rotor. In forward flight, however, these aerodynamic conditions are changing as a function of azimuthal location, since the resultant velocity vector changes based on the instantaneous location of the blade relative to the oncoming flow. This results in an unsteady loading on the rotor blade. Due to the fixed pitch nature of the rotor blades on the SUI Endurance (and on most multicopter platforms), the rotation rates of the individual rotors are also expected to change when transitioning between hover and forward flight. To assess these changes on the current vehicle platform, load cell data was monitored on the vehicle in hover and forward flight conditions until approximate trimmed conditions were obtained. These trim conditions were determined such that the pitch, roll, and yaw moments were nearly zero and the desired net thrust condition was achieved. A summary of the thrust conditions and target rotor rotation rates that achieved these trim conditions is provided in Table 2. As the data in the table show, trimmed hover conditions resulted in very similar target rotation rates for all four rotors. This is evidence of appropriate positioning of the load cell near the vehicle center of gravity since this would warrant very similar thrust generation from each rotor. Furthermore, forward flight conditions show a split between the forward and aft rotors in which the aft rotors continually exhibit higher rotation rates. The forward flight conditions also show very similar rotation rates between the two forward and aft rotor pairs (R1-R2, R3-R4), respectively. This is an indicator that the vehicle is laterally well-balanced. Note that for the remainder of this paper, only data for a net thrust condition of T_r =45 N will be presented. This is because these cases were the ones found to have minimal levels of acoustic contribution by the electric motors.

Table 2: Target vehicle thrust and rotor rotation rates for different flight conditions [Hover/Fwd. Flight].

	Rotor Rotation Rates (RPM)			
↓ Thrust, Rotor # →	R1	R2	R3	R4
$T_r = 27$ N	3634/3132	3645/3158	3703/3827	3701/3827
$T_r = 36$ N	4239/3610	4160/3641	4267/4425	4252/4412
$T_r = 45$ N	4655/4047	4622/3992	4720/4895	4697/4937

Figure 6(a) provides an on-axis flyover acoustics spectral comparison of hover and forward flight conditions for a common vehicle thrust of $T_r = 45$ N at a geometric observer location of $\theta_o = 70°$. Background noise spectra for hover and forward flight tunnel operation cases are also provided in this figure for reference. The hover spectrum displays a BPF of approximately 160 Hz that is shared among all four rotors. There is also a considerable amount of tonal content in the hover spectrum in the form of integer multiples of the BPF. The first six of these harmonics have amplitudes that are very comparable to the fundamental BPF. This is believed to be primarily due to rotor-airframe interaction noise. This source mechanism

has been previously identified to be responsible for higher harmonic acoustic content due to high-amplitude surface pressure fluctuations on a structure in close proximity to a hovering rotor blade.[5] On the current vehicle, the plane of the rotors is positioned approximately 15% of R above the airframe structures over which they pass.

The forward flight spectrum of Fig. 6(a) displays the division of BPFs between the forward and aft rotors, due to the rotation rate differences for this flight condition indicated in Table 2. These BPFs are of amplitudes approximately 15 dB greater than the BPF associated with the hover condition. Furthermore, the higher harmonics of these BPFs are seen to exhibit a gradual roll-off with increasing frequency. The spectrum is seen to be primarily broadband in nature for frequencies at and above 1 kHz. As will be seen in Section 3.3, this approximate frequency range of transition from periodic- to broadband-dominated noise is common to all measured polar angles for this forward flight condition.

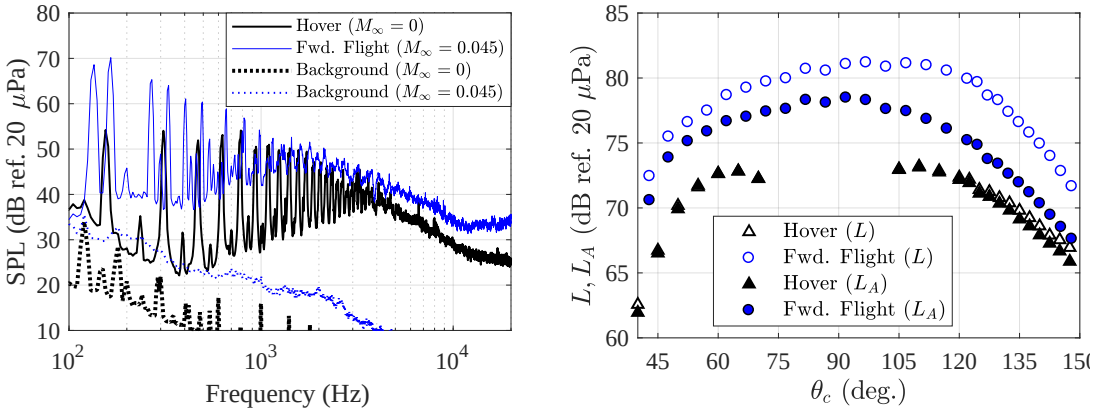

(a) On-axis flyover acoustic spectra ($\theta_o = 70°$) (b) On-axis flyover OASPL comparisons

Figure 6: On-axis flyover acoustic comparisons between hover and forward flight for $T_r = 45$ N. *Figure 6(b): Hover OASPLs not shown for* $75° \leq \theta_o \leq 100°$ *due to downwash contamination.*

Figure 6(b) provides a polar directivity comparison of the two flight conditions. It is important to note that the integrated levels for hover are not shown for $75° \leq \theta_o \leq 100°$, because of microphone signal contamination due to rotor wake downwash over the microphones. This rotor downwash effect is indicative of the resulting recirculation that is associated with the hover measurements in a partially enclosed environment, which is discussed further in Section 3.2. The results of Fig. 6(b) show considerably higher acoustic levels associated with the forward flight condition, both in terms of unweighted and A-weighted OASPLs. It is also interesting to note how application of A-weighting has almost no effect on the OASPL directivity behavior for hover, but a considerable impact on forward flight. As will also be discussed in Section 3.2, this is related to the nearly constant tonal acoustic energy present in the hover data over a broad frequency range, as compared to the majority of tonal energy in forward flight being concentrated at lower frequencies.

3.2 Periodic & Broadband Noise Contributions

As was shown in Fig. 6(a), the quadcopter exhibits a combination of periodic (tonal) and random (broadband) noise in both hover and forward flight conditions. It is useful to

quantitatively differentiate between these different noise sources for predictive validation purposes. Section 2.4 discussed methods to do this based on a periodic averaging of the acquired acoustic data on a rotor revolution basis (methods 2 and 3). While these techniques are useful, it is important to note their limitations. One important limitation is related to the fact that both hover and forward flight conditions result in multiple rotors operating at nearly the same condition and having very similar characteristic frequencies. This can result in constructive and destructive interference effects that can make these processing techniques inaccurate. Therefore, periodic averaging is limited to cases of either individual rotor operations in hover and forward flight or rotor fore-aft pair operations in forward flight. As will be shown, the latter set of cases are suitable for differentiating periodic and broadband noise because of the different rotation rates and associated frequencies of the forward and aft rotor for forward flight conditions.

Figure 7(a) provides a representation of the different post-processing techniques discussed in Section 2.4 applied to R1 in a hover condition. Several interesting observations can be made about the data in this plot. First, there is a considerable amount of tonal energy retained in the residual (broadband) spectrum of post-processing method 2. This is believed to be related to flow recirculation resulting from the static nature of the hover testing conditions (no wind tunnel flow). This in turn results in turbulent gust ingestion back into the rotor disk area which can manifest in the form of harmonic excitation. This could explain the additional tonal energy retained in the residual spectrum. Future prediction work will attempt to determine if this periodic extraction technique is suitable under these experimental conditions. For now, it is assumed that extracted BPF harmonic amplitudes are representative of the periodic behavior associated with the rotors. Figure 7(b) presents a comparison of the first 10 BPF harmonics between rotors R1 and R3. The purpose of this comparison is to identify acoustic differences between rotors spinning at very similar rotation rates subjected to different airframe conditions. As shown in Fig. 2, the airframe structure from which the aft rotor support arms extrude are considerably larger in planform area than those at the front of the vehicle. This implies that the aft rotors might be subjected to a larger flow disturbance due to rotor-airframe interactions than the forward rotors. The results of Fig. 7(b) confirm this, with the BPF harmonic spectrum of R3 containing much higher acoustic energy in the

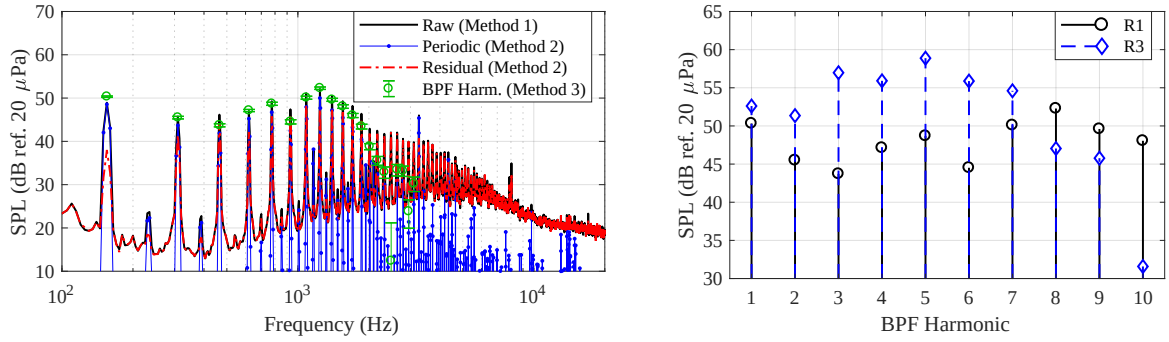

(a) R1 in hover

(b) BPF harmonics of R1 and R3

Figure 7: Periodic noise component extraction techniques applied to R1 and R3 under hover condition. *Note: Thrust condition of T_r = 45 N, on-axis flyover orientation at $\theta_o = 70°$.* Only the first 20 BPF harmonics extracted using method 3.

2nd through 7th BPF harmonics than that of R1. These results are consistent with those of Ref. 5.

Figure 8 presents the results of applying periodic-broadband extraction (method 2) for both individual operation cases of rotors R1 and R3 and for the simultaneous operation of these rotors (R1 & R3) in forward flight. This is done to determine the applicability of simple frequency-domain superposition of rotor sources for future noise prediction and modeling. As Figs. 8(a) and 8(b) show, the narrowband spectra results of the individual rotor operation cases are able to be effectively divided into periodic (tonal) and broadband noise contributions, with the slight exception of the R3 operation case having some tonal energy at the rotor BPF retained in the broadband spectrum. Similar results are obtained in Fig. 8(c) for the case of simultaneous operation of rotors R1 and R3. Periodic extraction for this case was done by performing two separate periodic averaging calculations: one using the rotation rate tracking data for R1, and the other for that of R3. The final periodic spectrum is the result of the addition of these two periodic spectra. The broadband spectrum for this case is then computed by assembling a composite spectrum from the smallest spectral amplitudes of the two residual spectra that result from this periodic averaging process.

Figure 8(d) provides a comparison between periodic A-weighted OASPL directivities computed by summation of the individual rotor operation cases (R1 + R3) and that computed from the case of simultaneous operation of the rotors (R1 & R3) in forward flight conditions. Furthermore, Fig. 8(e) provides the same comparison for broadband noise. It is interesting to observe that the periodic noise data for the two cases compare closely (to within 2 dB) for all measured observer angles, with the simultaneous operation data being consistently less than that for the summation case. The broadband noise, however, shows anywhere between a 3 and 5 dB difference in A-weighted OASPL between the two cases, with the simultaneous operation case data being consistently higher than that for the summation case. This is evidence of additional turbulent rotor wake interactions that occur for the case of simultaneous rotor operations that are not present during individual rotor operations. Finally, Fig. 8(f) provides a breakdown of periodic and broadband noise contributions for the individual rotor summation and simultaneous rotor operation cases at an observer angle of $\theta_o = 70°$. This plot is essentially a 1/3rd octave band representation of the periodic and broadband component data of Figs. 8(a)-8(c). This plot shows a transition from tonal-dominated to broadband-dominated noise at a 1/3rd octave band frequency of 1.25 kHz for the case of simultaneous rotor operation. This transition is not seen to occur until an approximate frequency of 2.5 kHz at a considerably lower acoustic amplitude for the individual rotor summation case. These results provide evidence that accurate prediction of the noise generated by a multirotor vehicle of this class warrants modeling of turbulent rotor wake interaction phenomena.

3.3 Integrated Level Directivity Trends

Figure 9 provides a summary of A-weighted OASPL directivities of the quadcopter at different azimuthal array orientations for both hover and forward flight conditions. It is interesting to note that while the on-axis flyover measurements exhibit considerably higher levels for the forward flight condition (as was described previously in Fig. 6(b)), the A-weighted acoustic levels are very similar between the two flight conditions for the bird's-eye orientation

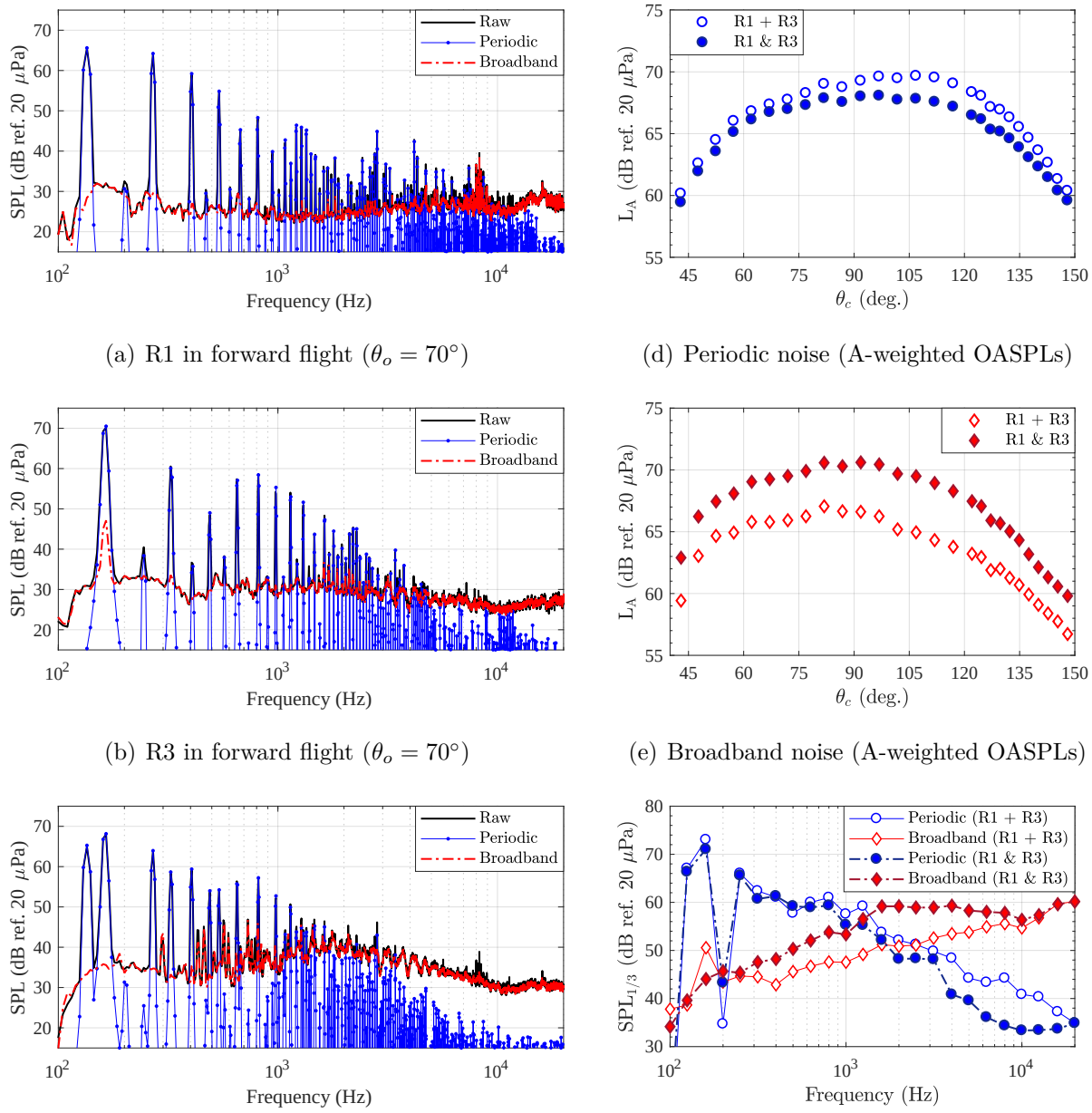

(a) R1 in forward flight ($\theta_o = 70°$)

(d) Periodic noise (A-weighted OASPLs)

(b) R3 in forward flight ($\theta_o = 70°$)

(e) Broadband noise (A-weighted OASPLs)

(c) R1&R3 in forward flight ($\theta_o = 70°$)

(f) R1+R3, R1&R3 components ($\theta_o = 70°$)

Figure 8: Periodic and broadband noise component extraction techniques applied to individual R1, R3 operations and simultaneous R1 & R3 operations in forward flight conditions. *Note: Thrust condition of T_r = 45 N, on-axis flyover orientation.*

($\phi = 130°$). Furthermore, both flight conditions display a common trend of smallest measured acoustic levels occurring for the sideline orientation (approximately coincident with the rotor plane). This is because unsteady loading noise — which can be due to a combination of unsteady rotor inflow conditions, rotor-airframe interactions, and rotor self-noise — is of highest amplitude out of the plane of the rotor. These results are in agreement with the trends identified in Refs. 4 and 5.

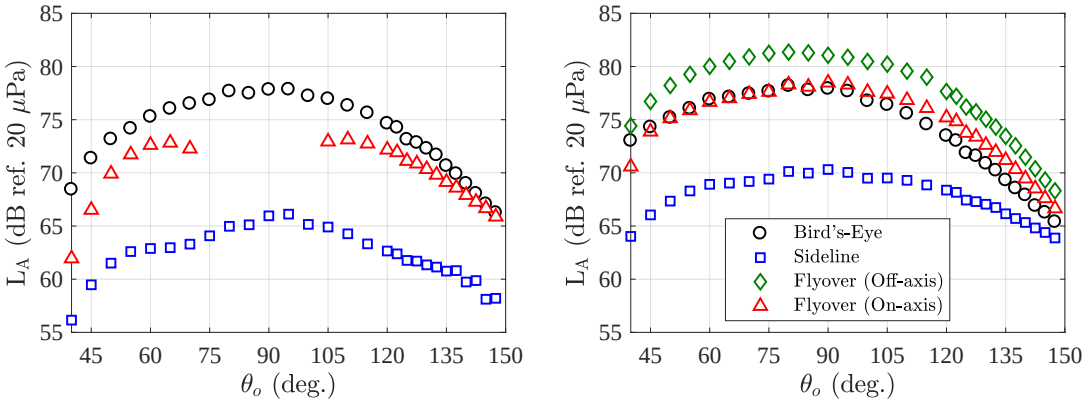

(a) Hover (b) Forward flight

Figure 9: A-weighted OASPL directivities of the SUI Endurance quadcopter in hover and forward flight conditions for different azimuthal array orientations. *Note: Thrust condition of $T_r = 45$ N; all rotors in operation. Figure 9(a): Hover OASPLs not shown for $75° \leq \theta_o \leq 100°$ due to downwash contamination.*

As is shown in Fig. 8(f), the forward-aft rotor pair R1 & R3 exhibits a transition from periodic- to broadband-dominated noise at a 1/3rd octave band frequency of 1.25 kHz. This is a useful observation because the cases in which all rotors are in operation prohibit the reliable utilization of the previously mentioned periodic/broadband noise extraction techniques. Therefore, a simple frequency parsing technique is implemented as an approximate means of determining the relative roles of periodic and broadband noise for the fully-operated vehicle. Figure 10 shows the result of this frequency parsing technique for an A-weighted OASPL calculation of periodic and broadband noise for the R1 & R3 simultaneous operation case in forward flight. The results show excellent agreement between these frequency-parsed OASPLs with those computed from the periodic and broadband noise extraction technique. Specifically, the approximated levels are within ±0.5 dB of the extracted values for all observer angles. This is therefore believed to be an appropriate method of approximating the relative roles of periodic and broadband noise for the case of full vehicle operation at this thrust condition. It is important to note that this method is not applicable to the other tested thrust conditions, nor is it applicable to other multicopter platforms of differing geometry.

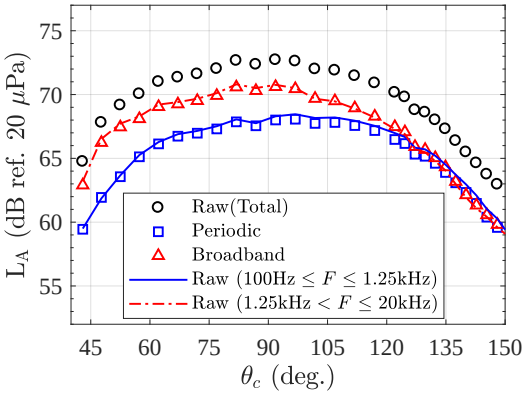

Figure 10: Relative roles of periodic and broadband noise for on-axis flyover L_A directivity of R1 & R3 in forward flight.

Finally, Fig. 11 provides an overview of the OASPL results using the previously discussed frequency parsing applied to the case of full vehicle operation. Note that it is assumed that the periodic noise of the system is approximately captured within the frequency range of $100\text{Hz} \leq F \leq 1.25\text{kHz}$, while broadband noise is captured within $1.25\text{kHz} < F \leq 20\text{kHz}$. These results are very interesting since they indicate that the relative importance of periodic

and broadband noise sources on the vehicle are heavily dependent on the noise metric. In other words, unweighted OASPLs indicate a comparable contribution of periodic and broadband noise for forward observer angles and periodic-dominated noise for aft observer angles. Meanwhile, A-weighted OASPLs indicate broadband-dominated noise for forward and overhead observer angles and a comparable contribution of periodic and broadband noise for aft observer angles. These latter observations are furthermore approximately consistent with the R1 & R3 results presented in Fig. 10. While these two noise metrics are not representative of other metrics that are based on time duration (such as EPNL and SEL), they do indicate a balanced importance of periodic and broadband noise source mechanisms for small UAS of this type.

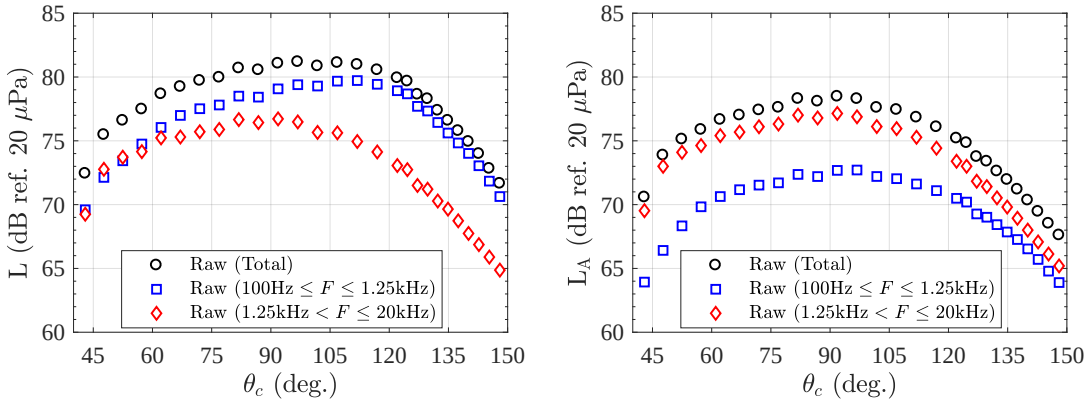

(a) Unweighted OASPL (b) A-weighted OASPL

Figure 11: On-axis flyover OASPL directivities of the SUI Endurance quadcopter in forward flight subjected to frequency parsing. *Note: Thrust condition of T_r = 45 N; all rotors in operation.*

4. CONCLUSIONS

This study investigates the acoustic characteristics of a representative multicopter system in simulated hover and forward flight conditions in an acoustic wind tunnel. The measurements encompassed a range of both microphone array orientations and net vehicle thrust conditions determined through the use of a multiaxis load cell. The primary goals of this study are to identify the interplay between different noise source mechanisms as well as to provide a data set against which future noise predictions may be compared. Trimming of the vehicle in hover revealed rotation rates approximately in common between all four rotors, indicating approximate positioning of the load cell near the vehicle center of gravity. Trimming of the vehicle in forward flight, meanwhile, resulted in a splitting of the rotation rates between the forward and aft rotors, with the aft rotors always operating at a higher rotation rate (approximately 20% faster) than the forward rotors. Forward flight conditions result in a different spectral character and increased flyover acoustic levels than those associated with hover conditions. Utilization of a periodic averaging technique allowed for tonal and broadband noise differentiation for cases of individual and fore-aft rotor pair operation cases in forward flight. This technique is not reliable for cases of full vehicle operation due to correlated rotor noise sources resulting from common rotation rates. However, simple frequency parsing is

used for these full vehicle cases to determine relative periodic and broadband noise levels based on the discussed periodic averaging technique results for rotor fore-aft pair cases. These results show a balance of importance between periodic and broadband noise sources for this vehicle, with the latter noise behavior evidenced to be strongly governed by rotor wake interaction phenomena in forward flight conditions. These results indicate that modeling of noise sources resulting from complex rotor wake and rotor-airframe interactions is warranted when considering acoustics as a design constraint for vehicles of this class.

ACKNOWLEDGMENTS

The authors would like to acknowledge Mr. John Swartzbaugh, Stanley Mason, and Bryan Lamb of the LSAWT at NASA Langley Research Center for their tireless efforts involving facility test setup and data acquisition. The authors would also like to acknowledge Mr. Harry Haskin of the LSAWT for the design of vehicle testing hardware. This work was funded by the NASA Convergent Aeronautical Systems (CAS) subproject, the Design Environment for Novel Vertical Lift Vehicles (DELIVER), the principal investigator of which is Dr. Colin Theodore.

REFERENCES

[1] S. Kesselman. *The First 1,000 Commercial UAS Exemptions*, Association for Unmanned Vehicle Systems International (AUVSI), (2016).

[2] R. Cabell, F. Grosveld, and R. McSwain. Measured noise from small unmanned aerial vehicles. In *Proceedings of NOISE-CON 2016*, volume 252, Providence, RI, p. 345-354, (2016).

[3] A. Christian and R. Cabell. Initial Investigation into the Psychoacoustic Properties of Small Unmanned Aerial System Noise. In *23rd AIAA/CEAS Aeroacoustics Conference*, Denver, CO, AIAA Paper 2017-4051, (2017).

[4] N. S. Zawodny, D. D. Boyd Jr., and C. L. Burley. Acoustic Characterization and Prediction of Representative, Small-Scale Rotary-Wing Unmanned Aircraft System Components. In *AHS International* 72$^{\text{nd}}$ *Annual Forum*, West Palm Beach, FL, (2016).

[5] N. S. Zawodny and D. D. Boyd Jr. Investigation of Rotor-Airframe Interaction Noise Associated with Small-Scale Rotary-Wing Unmanned Aircraft Systems. In *AHS International* 73$^{\text{rd}}$ *Annual Forum*, Fort Worth, TX, (2017).

[6] N. S. Zawodny and H. H. Haskin. Small Propeller and Rotor Testing Capabilities of the NASA Langley Low Speed Aeroacoustic Wind Tunnel. In *23rd AIAA/CEAS Aeroacoustics Conference*, Denver, CO, AIAA Paper 2017-3709, (2017).

[7] J. S. Bendat and A. G. Piersol. *Random Data Analysis and Measurement Procedures*, chapter 6: Statistical Errors in Advanced Estimates, pages 316–348. John Wiley & Sons Inc., 3rd edition, (2000).

[8] R. K. Amiet. Refraction of sound by a shear layer. *Journal of Sound and Vibration*, 58(4):467–482, (1978).

[9] R. L. Bennett and K. S. Pearsons. *Handbook of Aircraft Noise Metrics*. Canoga Park, CA, NASA CR 3406, (1981).